

Weak Electron-Phonon Coupling Is Insufficient to Generate Significant CISS in Two-Terminal Transport

Vipul Upadhyay^{1, 2, 3, a)} and Amikam Levy^{1, 2, 3, b)}

¹⁾Department of Chemistry, Bar-Ilan University, Ramat-Gan 52900, Israel

²⁾Institute of Nanotechnology and Advanced Materials, Bar-Ilan University, Ramat-Gan 52900, Israel

³⁾Center for Quantum Entanglement Science and Technology, Bar-Ilan University, Ramat-Gan 52900, Israel

A central open question in chiral-induced spin selectivity (CISS) is whether weak electron-phonon coupling in a helical molecular junction can generate a sizable spin polarization in two-terminal transport without invoking additional strong symmetry-breaking ingredients. We address this question by implementing a self-consistent nonequilibrium Green's function (NEGF) calculation for a helical tight-binding model with spin-orbit coupling and electron-phonon interactions. The electron-phonon self-energies are evaluated self-consistently, and the transport signal is extracted using the standard magnetization-reversal protocol with a spin-polarized analyzer lead. We benchmark a fully self-consistent NEGF within the self-consistent Born approximation (SCBA) treatment for both global and local electron-phonon couplings against commonly used approximations, including diagonal self-energy schemes. We quantify how the resulting transport regime and spin polarization depend on phonon frequency, coupling strength, bias, temperature, and system size. In contrast to large polarizations and anomalous size trends reported under approximate treatments, the fully self-consistent calculation yields negligible spin polarization, additionally the electron-phonon coupling mainly renormalizes the spectrum, and transport remains quasi-ballistic across the explored parameter range.

I. INTRODUCTION

The Chiral-Induced Spin Selectivity (CISS) effect, initially observed in transmission experiments^{1–5}, refers to the spin-based filtering or selectivity of electrons as they pass through chiral molecules, occurring even in the absence of external magnetic fields. Remarkably, reported spin polarizations can reach tens of percent^{1,2}, motivating potential applications, particularly in spintronics^{4,6,7}. From the moment the CISS effect was experimentally observed, theoretical efforts have been made to understand its microscopic origins^{8–11}. Spin-orbit coupling (SOC) emerged as a promising candidate to explain the phenomenon, due to its ability to mix spins of different orientations. However, because the CISS effect is typically observed in organic molecules, such as DNA, the SOC in these systems is generally weak and insufficient to explain the substantial spin polarization observed experimentally. As such, no widely accepted microscopic theory for CISS exists^{6,10}.

Any theoretical model considered should address the single-channel no-go theorem^{9,10}, which states that in strictly one-dimensional single-channel systems the SOC term can be gauged out of the Hamiltonian in the absence of spin-dependent potentials; therefore, SOC alone cannot produce robust spin-polarized transmission in such a minimal model. Furthermore, from a symmetry perspective, it is important to note that chirality breaks spatial inversion but does not, by itself, violate time-reversal symmetry (TRS)¹². Consequently, chirality alone cannot guarantee spin-selective transport in two-terminal setups, where Onsager reciprocity¹³ and Bardarson theorem¹⁴, enforce equal conductance for opposite

spin channels in the absence of explicit TRS breaking¹⁵. In many CISS experiments, however, spin-resolved signals are measured using magnetic or spin-projective contacts¹⁶, which already break TRS at the level of the leads or detectors. Within such setups, chirality can enable spin-selective transmission without violating global TRS, a viewpoint that underlies several recent theoretical approaches^{17–19}. One of the earlier theoretical studies based on these considerations was conducted by Guo et al.⁹, who observed relatively large spin polarization values on working with virtual Büttiker baths²⁰. However, the spin-orbit coupling (SOC) strength used in their model was 1–2 orders of magnitude higher than experimentally observed values. More recent approaches have explored various other methods to amplify the SOC strength, such as incorporating a feedback mechanism into the Schrödinger equation²¹, considering CISS as an interface effect^{22,23}, or attributing the amplification in spin polarization to nuclear motion²⁴.

A growing body of work suggests that sizeable CISS signals are difficult to account for within purely coherent single-particle descriptions, and may require additional ingredients beyond spin-orbit coupling alone, such as many-body interactions, environmental dephasing, or interfacial effects^{6,16,25–27}. A central open question in CISS is whether weak electron-phonon (e-ph) coupling can generate a sizable spin polarization in two-terminal transport without additional strong symmetry-breaking ingredients^{28–30}. This vibrational mechanism was predicted to amplify spin polarization by modifying the density of states for oppositely magnetized leads²⁸. However, these predictions were obtained using a non-self-consistent treatment of the interaction self-energies, which can violate conservation laws (e.g., current conservation) and introduce unphysical spectral features. Recent studies have revisited this mechanism using alternative approaches, including hierarchical equations of motion³⁰ and semiclassical treatments²⁹, and reported that large polarization may appear only

^{a)}Electronic mail: vipupadhyay4@gmail.com

^{b)}Electronic mail: amikam.levy@biu.ac.il

for individual trajectories³⁰ or during transient dynamics²⁹, while ensemble- or time-averaged steady-state polarization remains negligible.

Here we provide a controlled weak-coupling benchmark by solving the nonequilibrium Green's-function equations with e-ph self-energies evaluated fully self-consistently within the self-consistent Born approximation (SCBA)³¹. We consider both global and local e-ph couplings and explicitly compare the converged self-consistent solution to commonly used approximate schemes, including diagonal self-energy treatments. This enables a direct assessment of how approximation choices impact the transport regime and the inferred spin polarization.

The manuscript is organised as follows. We start by describing the model in the section II. We then discuss the relevant self-consistent NEGF equations used for analysing the model in the section III. This is followed by detailed discussion on obtained results, first the Energy-dependent results in the section IV, followed by the energy integrated results in the section V. Finally, we conclude in the section VI. A detailed derivation of all the equation used for the analysis can be found in the appendix A.

II. MODEL FOR VIBRATIONALLY AMPLIFIED CISS EFFECT

We begin by outlining Fransson's model for CISS (see Fig. 1). This model is based on a tight-binding Hamiltonian including chiral features, which are introduced due to the helical nature of the structure. This Hamiltonian is then augmented with spin-dependent electron-vibration interactions, which are indicated to enhance the spin polarization in the system. The Hamiltonian is explicitly written as²⁸,

$$\begin{aligned} \mathcal{H}_{\text{mol}} = & \sum_{m=1}^M \psi_m^\dagger \psi_m \left[\varepsilon_0 + \sum_\nu \varepsilon_\nu (a_\nu + a_\nu^\dagger) \right] + \sum_\nu \omega_\nu a_\nu^\dagger a_\nu \\ & - \sum_{m=1}^{M-1} \left(\psi_m^\dagger \psi_{m+1} + \text{H.c.} \right) \left[t_0 + \sum_\nu t_\nu (a_\nu + a_\nu^\dagger) \right] \\ & + \sum_{m=1}^{M-2} \left(i \psi_m^\dagger \mathbf{v}_m^{(+)} \cdot \boldsymbol{\sigma} \psi_{m+2} + \text{H.c.} \right) \left[\lambda_0 + \sum_\nu \lambda_\nu (a_\nu + a_\nu^\dagger) \right]. \end{aligned} \quad (1)$$

Here, ε_0 denotes the on-site energy of the electronic state at site m , and ψ_m^\dagger (ψ_m) are the creation (annihilation) operators for an electron at site m , with each ψ_m being a two-component spinor representing up and down spin. The vibrational modes are characterized by frequencies ω_ν , with a_ν^\dagger and a_ν denoting the phonon creation and annihilation operators, respectively. The parameter t_0 represents the nearest-neighbor hopping amplitude, while t_ν describes the e-ph-assisted hopping for mode ν . The spin-orbit coupling is captured by λ_0 , with λ_ν representing the e-ph-assisted spin-orbit term. To generalise the above model, we also modify it by adding a local on site e-ph interaction similar to the Holstein interaction^{32,33}, quantified by the parameter ε_ν .

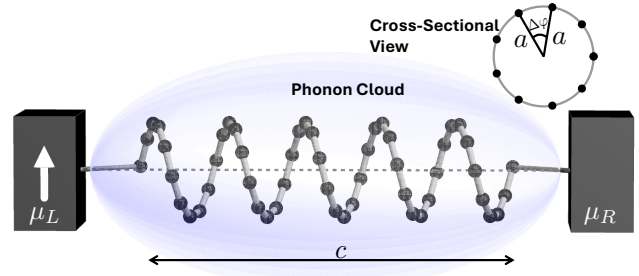


FIG. 1: Schematic of the theoretical setup. A helical molecule is kept between two leads with chemical potentials, $\mu_L = V/2$ and $\mu_R = -V/2$. The left lead is magnetised one way and the particle current is measured. The magnetization is then reversed and the current is measured again. The difference between the two currents quantifies the CISS-induced spin polarization. Specific parameters for this figure are $n_l = 10$, $m_l = 5$, radius of the helix $a = 1$, and length of the molecule $c = 8$.

The vector $\mathbf{v}_m^{(+)}$ defines the chirality of the spin-orbit interaction between next-nearest neighbors, and $\boldsymbol{\sigma}$ is the vector of Pauli matrices representing electron spin, with H.c. denoting the Hermitian conjugate. We work in the natural units so $e = 1$, $\hbar = 1$, $k_B = 1$. The chirality vector is defined as

$$\mathbf{v}_m^{(+)} = \hat{\mathbf{d}}_{m,1} \times \hat{\mathbf{d}}_{m+1,1}, \quad (2)$$

where $\hat{\mathbf{d}}_{m,s}$ is the unit vector along the bond connecting sites m and $m + s$, given by

$$\hat{\mathbf{d}}_{m,s} = \frac{\mathbf{r}_{m+s} - \mathbf{r}_m}{|\mathbf{r}_{m+s} - \mathbf{r}_m|}. \quad (3)$$

The positions of the sites in the helical structure are specified as,

$$\mathbf{r}_m = \left(a \cos \varphi_m, a \sin \varphi_m, \frac{(m-1)c}{M-1} \right), \quad (4)$$

where a is the radius of the helix, c is the length of the helix, M is the total number of sites, and $\varphi_m = \frac{2\pi(m-1)m_l}{M-1}$ is the azimuthal angle of site m , with $\Delta\varphi = \frac{2\pi m_l}{M-1}$, being the angular separation between two neighboring site. The helix consists of $M = m_l \times n_l$ sites, where m_l is the number of loops and n_l is the number of sites per loop (see Fig. 1). The analysis is carried out using the Nonequilibrium Green's Function (NEGF) under SCBA approach discussed below. These equations are derived using the Quantum Langevin Equation (QLE) approach^{34,35}. An explicit derivation of the used equation is given in the appendix A.

III. NONEQUILIBRIUM GREEN'S FUNCTION EQUATIONS

The QLE method is based on separating the different components of the dynamical equation of motion into dissipative and noise parts³⁴. Once this is achieved, it becomes possible

to calculate currents and density of states^{34,35}. For the given model, we have two real leads in the model through which the current is calculated using the usual Landauer-Büttiker formalism³⁵⁻³⁷. However, once we include the interactions with the environment using SCBA, the equations modify, and we need to solve them self-consistently. This involves effectively making a new virtual lead for e-ph interactions. The properties of this lead depend on the Green's Functions of the system, so we need to do self-consistent evaluations. We start by defining the retarded Green's Function G^R , which is the central quantity in any steady state NEGF analysis. For our case, the retarded Green's Function is,

$$G^R(E) = \left[E - H + \frac{i}{2}(\Gamma_L + \Gamma_R) - \Sigma_{\text{ph}}^R(E) \right]^{-1}, \quad (5)$$

where we assume a wide-band (flat-spectrum) approximation for the real leads²⁸. We define the phonon-induced broadening matrix by

$$\Gamma_{\text{ph}}(E) \equiv i \left[\Sigma_{\text{ph}}^R(E) - \Sigma_{\text{ph}}^A(E) \right], \quad (6)$$

which implies the standard Hilbert-transform relation³⁸

$$\Sigma_{\text{ph}}^R(E) = \frac{1}{2\pi} \mathcal{P} \int_{-\infty}^{\infty} dE' \frac{\Gamma_{\text{ph}}(E')}{E - E'} - \frac{i}{2} \Gamma_{\text{ph}}(E). \quad (7)$$

We assume the phonons are in thermal equilibrium at temperature T , i.e., their occupations are fixed to the Bose-Einstein distribution $n_B(\omega, T) = (e^{\omega/T} - 1)^{-1}$ (no nonequilibrium phonon heating). For compactness we define $n_\gamma \equiv n_B(\omega_\gamma, T)$ and use the shorthand $G_{\pm\gamma}^{</>}(E) \equiv G^{</>}(E \pm \omega_\gamma)$. The phonon broadening is then (see Appendix (A52))³¹

$$\begin{aligned} \Gamma_{\text{ph}}(E) = i \sum_\gamma M^\gamma & \left[(1 + n_\gamma) G_{-\gamma}^>(E) - n_\gamma G_{-\gamma}^<(E) \right] M^\gamma \\ & + i \sum_\gamma M^\gamma \left[n_\gamma G_{+\gamma}^>(E) - (1 + n_\gamma) G_{+\gamma}^<(E) \right] M^\gamma, \end{aligned} \quad (8)$$

where M^γ is the electron-phonon coupling matrix determined by the parameters $\varepsilon_\gamma, t_\gamma, \lambda_\gamma$.

Once $G^R(E)$ is known, the density of available states follows as,

$$\rho(E) = \frac{i}{2\pi} \text{Tr} [G^R(E) - G^A(E)] = \frac{i}{2\pi} \text{Tr} [G^>(E) - G^<(E)], \quad (9)$$

with $G^A(E) = G^R(E)^\dagger$. To compute particle currents we also require the occupied states,

$$\begin{aligned} G^<(E) = i G^R(E) & \left[f_L(E) \Gamma_L + f_R(E) \Gamma_R \right] G^A(E) \\ & + G^R(E) \Sigma_{\text{ph}}^<(E) G^A(E), \end{aligned} \quad (10)$$

where $f_\alpha(E) = [e^{(E-\mu_\alpha)/T} + 1]^{-1}$ is the Fermi-Dirac distribution of lead α and the phonon in-scattering self-energy is

(see Appendix (A53))³¹

$$\Sigma_{\text{ph}}^<(E) = \sum_\gamma M^\gamma [n_\gamma G_{-\gamma}^<(E) + (1 + n_\gamma) G_{+\gamma}^<(E)] M^\gamma. \quad (11)$$

Finally, the net particle current (incoming and outgoing) flowing out of lead α can be written in the interacting NEGF form^{39,40}, which we evaluate using the self-consistent Green's functions:

$$I_\alpha = \frac{i}{2\pi} \int_{-\infty}^{\infty} dE \text{Tr} \left\{ \Gamma_\alpha \left[f_\alpha G^>(E) + (1 - f_\alpha) G^<(E) \right] \right\}. \quad (12)$$

The CISS measurements are typically performed by comparing two transport experiments in which the spin polarization of one of the leads is reversed¹⁶. In our theoretical description, this procedure is implemented by modifying the spin-dependent broadening matrix of the left lead. Specifically, the non-zero elements are taken as,

$$\Gamma_{\uparrow\downarrow}^L = \Gamma_0 (1 \pm p), \quad (13)$$

where the polarization parameter takes opposite values, $p = \pm 0.5$, in the two experiments. The spin polarization is then extracted by comparing the resulting steady-state currents for the two lead polarizations, using the formula,

$$P_T = 100 \times \frac{I_\uparrow^L - I_\downarrow^L}{I_\uparrow^L + I_\downarrow^L} \quad (14)$$

For simplicity, the present analysis is restricted to a single phonon mode²⁸⁻³⁰, so $\varepsilon_\nu = \varepsilon_1, t_\nu = t_1, \lambda_\nu = \lambda_1$, and $\omega_\nu = \omega_0$. We now solve the above self-consistent equations to determine different physical quantities, and ultimately to calculate the spin polarization.

A. Details about numerical analysis

As evident from the previous section, the correct analysis of the model requires solving Eqs. (5)–(11) self-consistently. These coupled equations form a nonlinear, energy-dependent problem and are, in general, numerically challenging to solve⁴¹. To this end, we discretize the energy domain on a uniform grid with a spacing equal to the phonon frequency. This choice ensures that Green's functions connected via phonon absorption and emission processes are treated in a mutually consistent manner. The Green's functions and self-energies are obtained self-consistently through an iterative procedure until convergence is reached⁴¹. Since the total number of grid points is determined by the phonon frequency, we repeatedly shift the energy grid to effectively enhance the energy resolution and capture finer spectral features.

To improve convergence and suppress numerical instabilities, Pulay mixing algorithm⁴² is employed, wherein a linear combination of Green's functions from several previous

iterations is used to construct the next iterate. Convergence is monitored via the relative Frobenius norm of the residual between successive Green's functions, $\frac{\|G_{New}^R - G_{Old}^R\|}{\|G_{New}^R\|}$, with the

tolerance set to 5×10^{-5} . In Sections IV and V, we verify the physical validity of our analysis through several consistency checks, such as particle current conservation and the vanishing of current at zero bias.

Furthermore, the spin-polarization plots are obtained while explicitly accounting for residual numerical noise arising from the finite self-consistency tolerance. This noise is considered to be proportional to the sum of left, right, and phonon lead currents, which in the ideal case should give us zero. This tolerance leads to the appearance of sharp cutoffs in the polarization plots.

IV. ENERGY-DEPENDENT RESULTS

A. Global Interaction

We first discuss the results obtained when analysing Fransson's model²⁸, but solving it self-consistently. This means that the onsite e-ph interaction is turned off, $\epsilon_1 = 0$, and we only have hopping assistance due to the interactions. We call this the global (G) e-ph interaction model.

We start the analysis by studying the energy dependence of the density of states (DOS), shown in Fig. 2(a), calculated using Eq. (9). In the absence of interactions, the DOS exhibits several well-defined peaks corresponding to the eigenvalues of the non-interacting Hamiltonian. The finite width of these peaks arises from the coupling to the real leads, which introduces lifetime broadening and results in a continuous spectrum. When e-ph interactions are included, the DOS undergoes a marked qualitative change. Quantifying the strength of the e-ph interaction by χ , such that $t_1 = \chi t_0, \lambda_1 = \chi \lambda_0$, we see in Fig. 2(a) that as soon as the interactions are turned on, the peaks become broader while simultaneously their maximum value decreases. This trend keeps up with increasing χ , and for $\chi \sim 0.1$, the sharp resonant peaks present in the non-interacting case are strongly suppressed, and the DOS evolves into a much smoother profile. In particular, for larger e-ph interaction, a broad plateau develops in the central energy region, with the spectral density gradually decreasing on either side. Compared to the non-interacting case, the overall DOS is significantly broadened, indicating that electron-phonon coupling leads to a substantial redistribution of spectral weight over energy. This overall trend is partially similar to the behavior reported in the study²⁸, where electron-phonon interactions also lead to significant modification of the spectral features. However, there are important qualitative differences between the two treatments. In the earlier study, the individual resonant peaks remain clearly visible even in the presence of stronger interactions (see Fig. 5(a) in Appendix B 1), whereas in our fully self-consistent calculation, these peaks are largely washed out. This distinction suggests that the degree of self-consistency and the treatment of interactions play a crucial role in determining the resulting spectral properties.

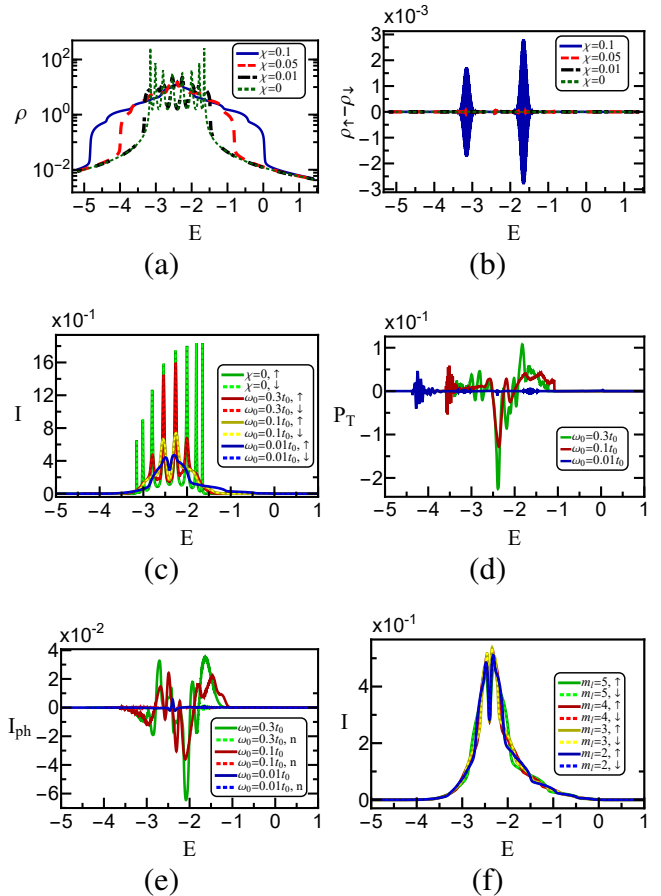


FIG. 2: Energy-dependent Figures with Global e-ph interaction: (a) Variation of density of states for different e-ph interaction strength χ , such that $t_1 = \chi t_0, \lambda_1 = \chi \lambda_0$. (b) Difference in density of electronic states for opposite lead magnetization, $\rho_\uparrow - \rho_\downarrow$, for different e-ph interaction strengths. (c) Variation of particle current coming out of the left bath, for opposite lead magnetization and different phonon frequencies. (d) Energy-dependent Spin polarization for different phonon frequencies. (e) Energy-dependent Phonon-bath current and numerical current noise denoted by the symbol 'n' for different phonon frequencies and left lead polarisation, $p=0.5$. The numerical noise is defined in the subsection III A. (f) Energy-dependent current for different system sizes. The default system size considered above is $n_l = 4, m_l = 2$. The e-ph coupling is similar to the study²⁸, with $\epsilon_1 = 0$, and the default values of the parameters used in the model and the code in units of 0.1 ev are $t_0 = 0.4, \epsilon_0 = -6t_0, t_1 = 0.1t_0, \lambda_0 = t_0/40, \lambda_1 = 0.1\lambda_0, \Gamma_0 = t_0/4, \omega_0 = 0.01t_0, T = 0.25$ (300K). Also, radius and length of helix are equal, $a = c = 1$. The chemical potentials of the two leads are given as, $\mu_L = V/2, \mu_R = -V/2$, and $V = 15t_0$.

To explore the implications of these changes for spin-dependent effects, we next plot the difference in the DOS for opposite lead magnetizations in Fig. 2(b). The resulting difference remains small across the entire energy range and does not show pronounced features that would indicate favorable conditions for the emergence of significant spin polarization. This is an interesting result, as it contrasts with the conclusions drawn in earlier studies^{28,43}, where larger spin-

dependent DOS differences were reported.

We then examine the transport properties by analyzing the energy-resolved particle current flowing out of the left lead, evaluated using the integrand of Eq. (12). This energy-dependent particle current for different phonon frequencies is shown in Fig. 2(c). We observe that with increasing phonon frequency, the peak magnitude of the particle current increases, accompanied by progressively sharper and more well-defined spectral peaks. This is because for smaller frequencies, the Green's Functions which are very close in energy are interconnected, and the self-consistent evaluation washes out individual special points of the discrete Hamiltonian, and the peaks settle down into smoother curves. On the other hand, when the phonon frequencies are larger, the Green's Functions are connected over a much larger energy range, and hence the self-consistent evaluation still keeps the local special energy points of the original discrete Hamiltonian. However, the energy-dependent lead currents corresponding to opposite lead magnetizations are visually indistinguishable over the entire energy window considered for the different phonon frequencies. This absence suggests that reversing the lead magnetization has a negligible effect on the transport characteristics, which serves as an important benchmark for a CISS setup.

This observation is further confirmed by the corresponding polarization plot shown in Fig. 2(d), where the spin polarization remains quite small at all energies for the different frequencies considered. As discussed earlier in the subsection III A, these polarization plots are obtained while accounting for residual numerical noise. This tolerance leads to the appearance of sharp cutoffs observed.

The current contribution arising specifically from e-ph coupling is shown in Fig. 2(e). We find that the inelastic current associated with e-ph interactions is negligibly small at low phonon frequencies when compared to the current through the real leads. However, this contribution increases with increasing phonon frequency, indicating that low-frequency phonons are absorbed less efficiently than higher-frequency modes. Although the resulting phonon-bath currents remain smaller than the real lead current, they are not negligible, consistent with expectations in the weak e-ph coupling regime.

We also observe a correlation between the energy dependence of the e-ph current and the polarization profile shown in Fig. 2(d), with larger phonon-bath currents generally corresponding to enhanced polarization. However, because the phonon currents exhibit oscillatory behavior enforced by the overall current-conservation condition, $I_L = I_R$, similar oscillations appear in the polarization curve. This indicates that the net polarization, obtained after averaging over energy, is expected to be significantly smaller than the magnitude suggested by the individual peaks. A detailed discussion of this effect is deferred to Sec. V. In the same figure 2(e), we also display the numerical noise associated with these calculations, estimated by the sum of the left, right, and phonon-bath currents, which should vanish in the ideal limit. We find that this quantity remains negligibly small compared to the physical current signals, thereby confirming the numerical stability and reliability of our results.

Finally, by plotting the left-lead current for different system sizes in Fig. 2(f), we observe that the energy-dependent current profiles do not change significantly with system size, indicating quasi-ballistic transport in the setup. This suggests that the e-ph coupling primarily leads to spectral renormalization and phase loss, rather than momentum loss. Suspecting that the global nature of the e-ph interaction may be responsi-

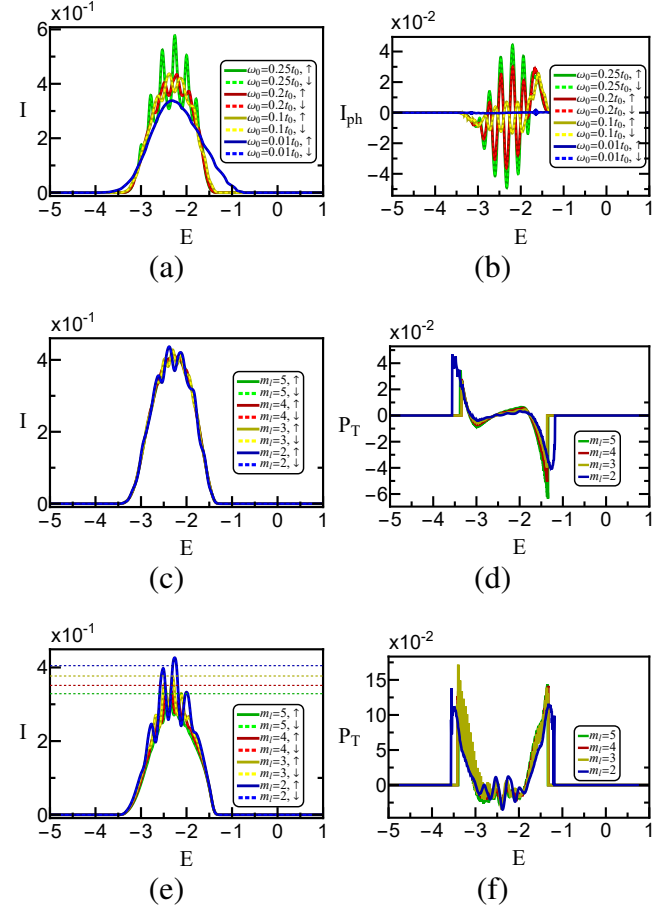


FIG. 3: Energy-dependent figures with local e-ph interaction: (a) Variation of Energy-dependent particle current coming out of the left bath, for opposite lead magnetization and different phonon frequencies. (b) Variation of phonon-bath current with energy for different phonon frequencies (c) Energy-dependent left lead particle current for different system sizes, and (d) Variation of polarization with energy for different system sizes. Currents characteristics under the diagonal approximation described in subsection IV C, (e) Energy-dependent left lead particle current for different system sizes with diagonal approximation, the horizontal dashed lines show the energy integrated particle current for their respective system size, (f) Energy-dependent polarization for the case with diagonal approximation. As earlier, the default system size considered above is $n_l = 4, m_l = 2$. The default values of the parameters used in the model and the code in units of 0.1 eV are $t_0 = 0.4, \epsilon_0 = -6t_0, \epsilon_1 = 0.1t_0, \lambda_0 = t_0/40, \lambda_1 = 0.1\lambda_0, \Gamma_0 = t_0/4, \omega_0 = 0.1t_0, T = 0.25$ (300 K). Also, $t_1 = 0.1t_0$ for the mixed coupling with diagonal approximation figs, while it is '0' for the purely local case. The chemical potentials of the two leads are given as $\mu_L = V/2, \mu_R = -V/2$, and the voltage is $V = 15t_0$.

ble for this behavior, we next study a more local model with on-site e-ph interactions. The results of this analysis are discussed in the following subsection.

B. Behavior with local interaction

We next examine how the transport behavior changes when a Holstein-like on-site e-ph interaction³² with $\varepsilon_1 \neq 0$ is introduced. For this case, we set the spin-independent hopping parameter to zero, $t_1 = 0$, while keeping the spin-dependent e-ph interaction finite, $\lambda_1 \neq 0$, and refer to this setup as the local (L) case.

In Fig. 3(a), we plot the current for different phonon frequencies. As in the global interaction case, the current spectrum becomes progressively smoother as the phonon frequency is reduced. Figure 3(b) further shows that, even for local coupling, phonon absorption increases with increasing phonon frequency. The dependence of the current on system size is shown in Fig. 3(c). Here again, the energy-resolved current spectrum shows little variation with system size, indicating that the transport remains quasi-ballistic. This suggests that, even for local e-ph interactions, momentum relaxation is weak and the dominant effect of the coupling is spectral renormalization and phase loss. A similar behavior has been reported for a dephasing model previously⁴⁴, where a self-consistent treatment using the full corrective matrices leads to only phase loss while preserving momentum conservation. Despite the presence of a non-negligible phonon bath contribution to the electron current in all the cases discussed above, we find that the particle currents corresponding to opposite lead magnetizations remain nearly indistinguishable. This indicates that weak e-ph coupling, even in the presence of local Holstein interactions and spin-dependent hopping, is insufficient to induce a significant CISS effect in chiral molecules. This conclusion is further supported by the polarization plotted for different system sizes in Fig. 3(d).

Suspecting that the quasi-ballistic transport behavior observed in global and local cases is the reason for small spin polarization, we implement a diagonal approximation, similar to that employed in Ref. ⁴⁴, in the following subsection.

C. Mixed coupling with diagonal approximation

To explore the impact of enhanced dephasing on transport, we now adopt a diagonal approximation for the electron-phonon self-energies, keeping only the diagonal elements of the lesser and greater Green's functions in Eq. (11). The resulting e-ph-dependent matrices are then used in the retarded Green's function of Eq. (5), again retaining only the diagonal contributions. This approach makes the setup analogous to Büttiker voltage probes^{44,45}, effectively introducing phase-breaking as well as momentum breaking processes, and reducing the electronic mean free path. As a result, the system is expected to leave the quasi-ballistic regime and enter a super-diffusive transport regime. For this case, we consider a generalized electron-phonon coupling where all the e-ph coupling

parameters, ε_1 , t_1 , and λ_1 , are nonzero.

In Fig. 3(e), we plot the current profile for different system sizes. In this case, the current decreases with increasing system size, although the reduction does not follow an exact $1/N$ scaling, indicating that the system is in a regime between ballistic and diffusive transport, i.e., the super-diffusive regime. The corresponding polarization, shown in Fig. 3(f), increases slightly with system size, but the enhancement is still not sufficient to produce large spin polarizations. In the next section, we examine the energy-integrated behavior for all the cases considered till now.

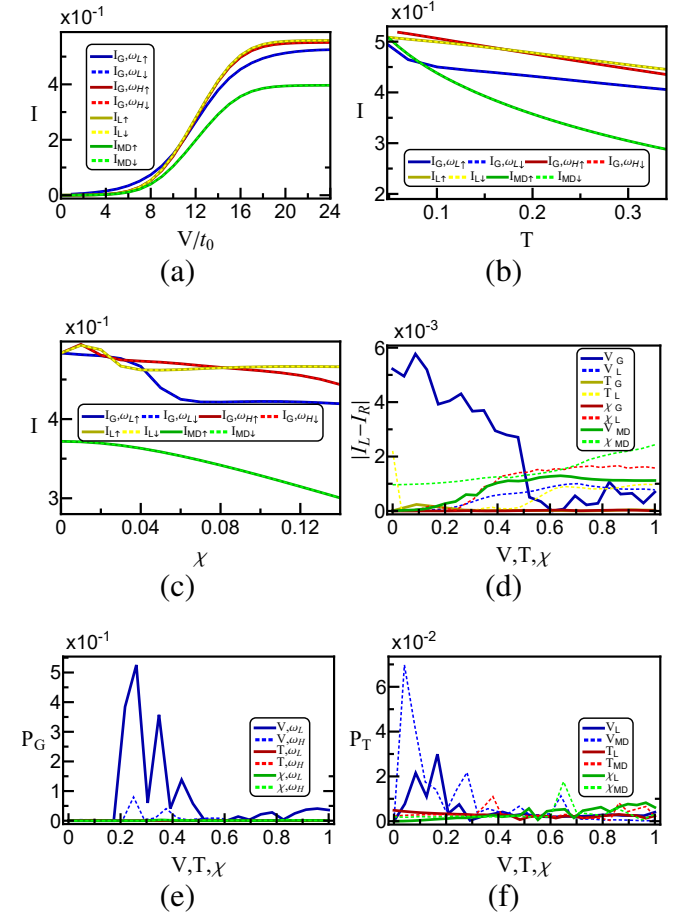


FIG. 4: Energy integrated figures: (a) Variation of particle current for global (G), local (L), and mixed-diagonal (MD) couplings with voltage. For the global case, two different phonon frequencies are considered, ' $\omega_0 = \omega_L = 0.01t_0, \omega_0 = \omega_H = 0.1t_0$ ', for the other two cases the phonon frequency is $\omega_0 = 0.1t_0$. Variation of particle current with (b) Temperature, and (c) e-ph coupling strength χ . (d) Difference between left and right bath current with normalised Voltage, Temperature, and χ . The x-axis for the different parameters has been normalised according to their respective ranges, as shown in earlier graphs. polarization plots with normalised Voltage, Temperature, and e-ph interaction strength for (e) global coupling, (f) Local coupling, and mixed coupling with Diagonal Approximation. The default parameters for Global and Local figures are the same as stated in earlier figures. For Mixed-Diagonal, we use the system size $m_l = 5, n_l = 4$.

V. ENERGY INTEGRATED BEHAVIOR

Finally, we study the energy-integrated total currents for the three types of interactions discussed in the previous section: the Fransson-like global e-ph interaction (G), the Holstein-like local interaction with spin-dependent nearest-neighbor hopping (L), and the mixed coupling with the diagonal approximation (MD). This energy-integrated current corresponds to the quantity typically measured in CISS experiments¹⁶ and is directly related to the magnitude of the CISS effect.

We begin by plotting the energy-integrated currents as a function of voltage in Fig. 4(a). As expected, the particle currents are zero in the absence of a chemical potential difference between the leads. With increasing voltage, the currents rise non-monotonically and eventually saturate at higher voltages. For all interaction models, the particle currents under opposite lead magnetizations remain visually indistinguishable. This indicates that, irrespective of the interaction type or the amount of phonon absorption, the CISS effect remains negligible in the weak e-ph coupling regime.

Figure 4(b) shows the currents as a function of temperature. As anticipated, the currents decrease with increasing temperature due to enhanced thermal fluctuations⁴⁶. Examining the currents as a function of the e-ph coupling strength parameter χ in Fig. 4(c), we observe a general decrease, consistent with dissipation induced by interactions. Interestingly, for very weak coupling and relatively larger frequency ($\omega_0 = 0.1t_0$), the currents show a modest increase for both the global and local interactions. This counterintuitive enhancement, where weakly opening the inelastic channel increases the current, has been reported previously³¹.

Based on these results, even at the energy-integrated level, the currents for opposite lead magnetizations remain nearly identical across all parameter regimes. This reinforces the conclusion that the present model does not produce significant spin polarization under weak e-ph coupling. To further validate our numerics, we verify current conservation by plotting the difference between the left and right bath currents in Fig. 4(d). The x-axis is normalized for all parameters between 0 and 1. We find that the difference remains negligibly small across the entire parameter range, confirming that the left and right currents are equal within numerical tolerance, a nontrivial consistency check of our implementation.

We also plot the corresponding spin polarization for all parameters (V, T, χ). In Fig. 4(e), the global interaction results show very small polarization. Notably, the energy-integrated polarization is smaller for higher-frequency phonons, despite their larger phonon currents, indicating that the correlation between phonon currents and polarization seen in energy-resolved results does not persist after integration. Figure 4(f) shows the polarization for the local and mixed-diagonal cases, which remain similarly negligible. Overall, even the integrated currents exhibit minimal spin polarization.

All our results indicate that, within SCBA and weak electron-phonon coupling, the molecular model considered here is insufficient to produce observable CISS effects. The lack of significant spin polarization suggests that additional physical ingredients or more advanced treatments beyond SCBA may be necessary to capture the essential mechanisms underlying chiral-induced spin selectivity.

VI. CONCLUSION

We investigated spin polarization in electron transport through a helical molecular junction coupled to vibrational modes, focusing on a widely used vibrational mechanism proposed to enhance CISS²⁸. In contrast to previous studies, we solved the NEGF equations fully self-consistently within the self-consistent Born approximation (SCBA), thereby avoiding uncontrolled evaluation of the electron-phonon self-energies. Within this weak-coupling framework, the resulting steady-state spin polarization is strongly suppressed and remains negligible over a wide range of parameters. Our results therefore, constrain vibrationally assisted CISS in two-terminal, single-orbital junction models in the weak electron-phonon coupling regime.

We performed the analysis for three electron-phonon coupling schemes: global, local, and a mixed scheme employing a diagonal self-energy approximation. For both the global and local couplings, electron-phonon interactions primarily renormalize the electronic spectrum, and the current exhibits only a weak dependence on system size, consistent with predominantly quasi-ballistic transport. In contrast, introducing the diagonal approximation qualitatively alters the size dependence of the current, producing a pronounced decrease with increasing system size. Importantly, across all three schemes, the energy-integrated spin polarization remains very small. Although the energy-resolved calculations can show localized polarization features (in some cases correlated with phonon-bath currents), these features are strongly suppressed upon energy integration.

Since the weak-coupling, two-terminal models studied here do not yield a sizable steady-state polarization even when the transport regime changes under approximations, it is natural to seek additional mechanisms. Possible missing ingredients include multi-orbital structure^{16,19}, stronger-coupling effects, electron-electron interactions, or explicitly nonequilibrium spin-dependent environments.

VII. ACKNOWLEDGEMENT

VU thanks Lev Kantorovich for his suggestion of using Pulay method for numerical convergence. This research was supported by the ISF Grants No. 3105/23.

Appendix A: Derivation of the NEGF equations using the Quantum Langevin Equation Approach

We try to derive the relevant equation of motion for our study using the so called Quantum Langevin equation method pioneered by Dhar et. al³⁴. Specifically, major part of this derivation is similar to the one presented in the book³⁵. To start, we consider a molecular junction consisting of a molecule that is coupled to two electronic reservoirs (left and right leads), while interacting with vibrational degrees of freedom (phonons). Throughout we set $\hbar = 1, k_B = 1$ and adopt the Heisenberg picture where the time-evolution of an operator \hat{O} is governed by,

$$\frac{d\hat{O}}{dt} = i[H_{\text{tot}}, \hat{O}]. \quad (\text{A1})$$

The total Hamiltonian is written as a sum of five contributions,

$$H_{\text{tot}} = H_{\text{el}} + H_{\text{ph}} + H_{\text{el-ph}} + H_{\text{leads}} + H_{\text{e-lead}}, \quad (\text{A2})$$

each of which is defined explicitly below. The molecule is modeled using a tight-binding representation,

$$H_{\text{el}} = \sum_{i,j} H_{ij} c_i^\dagger c_j, \quad (\text{A3})$$

where c_i^\dagger (c_i) creates (annihilates) an electron on molecular site i , and H_{ij} describes onsite energies and coherent hopping amplitudes within the molecular structure. The molecular vibrations are described as independent harmonic oscillators,

$$H_{\text{ph}} = \sum_{\beta} \omega_{\beta} \left(b_{\beta}^\dagger b_{\beta} + \frac{1}{2} \right), \quad (\text{A4})$$

where b_{β}^\dagger (b_{β}) creates (annihilates) a phonon in mode β of frequency ω_{β} . We consider linear coupling between the electronic density matrix and phonon displacements,

$$H_{\text{el-ph}} = \sum_{i,j,\beta} M_{ij}^{\beta} c_i^\dagger c_j (b_{\beta}^\dagger + b_{\beta}), \quad (\text{A5})$$

where M_{ij}^{β} denotes the coupling matrix elements. We assume M^{β} to be Hermitian, ensuring the overall Hamiltonian is Hermitian. The electronic reservoirs are taken as non-interacting Fermi seas in thermodynamic equilibrium at their respective chemical potentials μ_L and μ_R ,

$$H_{\text{leads}} = \sum_{\alpha} \varepsilon_{\alpha}^L c_{\alpha}^\dagger c_{\alpha} + \sum_{\alpha'} \varepsilon_{\alpha'}^R c_{\alpha'}^\dagger c_{\alpha'}, \quad (\text{A6})$$

with c_{α} ($c_{\alpha'}$) denoting annihilation operators in the left (right) lead. Electron tunneling between molecule and reservoirs is described by,

$$H_{\text{e-lead}} = \sum_{i,\alpha} \left(V_{i\alpha}^L c_i^\dagger c_{\alpha} + \text{h.c.} \right) + \sum_{i,\alpha'} \left(V_{i\alpha'}^R c_i^\dagger c_{\alpha'} + \text{h.c.} \right). \quad (\text{A7})$$

We now derive the operator equations of motion. Applying the Heisenberg equation to the molecular annihilation operator yields

$$\begin{aligned} \dot{c}_i(t) = & -i \sum_j H_{ij} c_j(t) - i \sum_{j\beta} M_{ij}^{\beta} c_j(t) (b_{\beta}^\dagger(t) + b_{\beta}(t)) \\ & - i \sum_{\alpha} V_{i\alpha}^L c_{\alpha}(t) - i \sum_{\alpha'} V_{i\alpha'}^R c_{\alpha'}(t). \end{aligned} \quad (\text{A8})$$

It is useful to rewrite this compactly in vector notation as

$$|\dot{c}(t)\rangle = -iH|c(t)\rangle - i \sum_{\beta} M^{\beta} (|c(t)b_{\beta}\rangle + |c(t)b_{\beta}^\dagger\rangle) - iV^L|c(t)\rangle_L - iV^R|c(t)\rangle_R, \quad (\text{A9})$$

where the vectors encode the molecular, left-lead, and right-lead operators.

The corresponding equations for the lead fermions read

$$\dot{c}_\alpha(t) = -i\varepsilon_\alpha^L c_\alpha(t) - i \sum_j V_{j\alpha}^{L*} c_j(t), \quad (\text{A10})$$

$$\dot{c}_{\alpha'}(t) = -i\varepsilon_{\alpha'}^R c_{\alpha'}(t) - i \sum_j V_{j\alpha'}^{R*} c_j(t), \quad (\text{A11})$$

while those for the phonon operators are

$$\dot{b}_\beta(t) = -i\omega_\beta b_\beta(t) - i \sum_{ij} M_{ij}^\beta c_i^\dagger(t) c_j(t), \quad (\text{A12})$$

$$\dot{b}_\beta^\dagger(t) = i\omega_\beta b_\beta^\dagger(t) + i \sum_{ij} M_{ij}^\beta c_i^\dagger(t) c_j(t). \quad (\text{A13})$$

Equations (A8) form the starting point for our non-equilibrium quantum transport analysis. In the following, we formally solve the reservoir and phonon equations and substitute the results into (A8). This yields a closed integro-differential quantum Langevin equation for the molecular operators, which can then be systematically mapped to the standard NEGF formulation.

Solving the lead equation of motion (EOM)

The left-lead operators satisfy the vector equation

$$|\dot{c}(t)\rangle_L = -iH^L|c(t)\rangle_L - iV^{L\dagger}|c(t)\rangle, \quad (\text{A14})$$

where H^L is the single-particle Hamiltonian of the left lead and V^L the molecule–left-lead coupling matrix. The homogeneous part gives the free evolution,

$$|c^{(0)}(t)\rangle_L = e^{-iH^L(t-t_0)}|c(t_0)\rangle_L. \quad (\text{A15})$$

The inhomogeneous equation can be solved using the integrating-factor method, which yields

$$|c(t)\rangle_L = |c^{(0)}(t)\rangle_L - i \int_{t_0}^t dt' e^{-iH^L(t-t')} V^{L\dagger} |c(t')\rangle. \quad (\text{A16})$$

We identify the retarded Green's function (matrix) of the left lead as

$$g^L(t-t') \equiv -i\Theta(t-t') e^{-iH^L(t-t')}. \quad (\text{A17})$$

An entirely analogous expression holds for the right lead,

$$|c(t)\rangle_R = |c^{(0)}(t)\rangle_R - i \int_{t_0}^t dt' e^{-iH^R(t-t')} V^{R\dagger} |c(t')\rangle, \quad (\text{A18})$$

with the corresponding retarded Green's function $g^R(t-t') = -i\Theta(t-t') e^{-iH^R(t-t')}$.

To derive the equation of motion for the fermionic operators of the molecule, we substitute these solutions into the system EOM and separate the lead contribution into two parts:

1. a noise term depending on the initial lead operators $|c(t_0)\rangle_{L,R}$,
2. a damping term involving integrals over past system operators $|c(t')\rangle$.

Following the standard quantum Langevin approach (see, e.g.,³⁴), we define the **lead noise operators** as

$$|\eta_L(t)\rangle = iV^L g^L(t-t_0) |c(t_0)\rangle_L, \quad |\eta_R(t)\rangle = iV^R g^R(t-t_0) |c(t_0)\rangle_R. \quad (\text{A19})$$

These terms account for random fluctuations originating from the leads in the distant past ($t_0 \rightarrow -\infty$). Their ensemble averages vanish,

$$\langle \eta_{L,R,\alpha}(t) \rangle = 0,$$

while their correlations determine the statistical properties of the reservoirs.

Next, we define the **lead self-energy kernels** as,

$$\Sigma_L^r(t-t') = V^L g^L(t-t') V^{L\dagger}, \quad \Sigma_R^r(t-t') = V^R g^R(t-t') V^{R\dagger}. \quad (\text{A20})$$

Substituting everything into the equation of motion (A8), we obtain,

$$\begin{aligned} |\dot{c}(t)\rangle &= -iH|c(t)\rangle - i|\eta_L(t)\rangle - i \int_{t_0}^t dt' \Sigma_L^r(t-t')|c(t')\rangle - i|\eta_R(t)\rangle - i \int_{t_0}^t dt' \Sigma_R^r(t-t')|c(t')\rangle \\ &\quad + \text{Phonon terms.} \end{aligned} \quad (\text{A21})$$

The above equation is a quantum Langevin equation for the system fermions, with explicit noise terms $|\eta_{L,R}\rangle$ and memory kernels $\Sigma_{L,R}^r$ describing dissipation due to the real leads. Once we know these contribution we can directly write the steady state in scattering and broadening matrices for an energy ‘E’ due to the real leads, using the relations³⁴,

$$\Sigma_{L,i}^<(E) = i\langle \tilde{\eta}_{L,j}^\dagger(E) \tilde{\eta}_{L,i}(E) \rangle \quad (\text{A22})$$

where, $\tilde{\eta}_{L,j}(E)$ is the j^{th} component of the Fourier transform of the noise vector. Here, $\Sigma_L^<(E) = if_L(E)\Gamma_L$, as the left lead has well defined chemical potential. Similarly we can also find the broadening matrix using the retarded kernel,

$$\Gamma_L(E) = i(\tilde{\Sigma}_L^r(E) - \tilde{\Sigma}_L^a(E)) \quad (\text{A23})$$

Again a function of $\tilde{\Sigma}_L^r(E)$ signifies Fourier transform of the damping kernel, $\tilde{\Sigma}_L^a(E) = \tilde{\Sigma}_L^{r\dagger}(E)$. Once we have both the contribution, we can find the particle current at an energy ‘E’, using the equations presented in the section III. We are assuming a flat spectrum so, Γ_L is a constant diagonal matrix with non-zero elements only at first and second diagonal, these element are proportional to the square of system-lead coupling. Similar relations hold for the right lead terms. In the following section, we try to write the contributions due to e-ph coupling.

Solving the electron–phonon equation of motion (EOM)

We now analyze the dynamics of composite operators involving one electron and one phonon. This will allow us to identify the phonon-induced noise and damping acting on the electronic system. We define,

$$C_{n\gamma}^{ph}(t) \equiv c_n(t) b_\gamma(t), \quad (\text{A24})$$

and similarly, later, $K_{n\gamma}^{ph}(t) \equiv c_n(t) b_\gamma^\dagger(t)$. The time derivative of $C_{n\gamma}^{ph}$ follows from the product rule:

$$\frac{d}{dt}(c_n b_\gamma) = \dot{c}_n b_\gamma + c_n \dot{b}_\gamma. \quad (\text{A25})$$

Using the equations of motion for c_n and b_γ we obtain

$$\begin{aligned} \frac{d}{dt}(c_n b_\gamma) &= \left(-i \sum_j H_{nj} c_j - i \sum_{j\beta} M_{nj}^\beta c_j (b_\beta^\dagger + b_\beta) - i \sum_\alpha V_{n\alpha}^L c_\alpha - i \sum_{\alpha'} V_{n\alpha'}^R c_{\alpha'} \right) b_\gamma \\ &\quad + c_n \left(-i\omega_\gamma b_\gamma - i \sum_{ij} M_{ij}^\gamma c_i^\dagger c_j \right). \end{aligned} \quad (\text{A26})$$

We neglect direct lead–phonon terms, ‘ $c_\alpha b_\gamma$ ’, since phonons couple only to the molecular fermions and not lead fermions, and we expect their correlation to go to zero $\langle c_\alpha b_\gamma \rangle \approx 0$. Using these approximations, we separate the free part of (A26) and move it to the left-hand side:

$$\frac{d}{dt} C_{n\gamma}^{ph}(t) + i\omega_\gamma C_{n\gamma}^{ph}(t) + i \sum_j H_{nj} C_{j\gamma}^{ph}(t) = -i \sum_{j\beta} M_{nj}^\beta (b_\beta^\dagger + b_\beta) b_\gamma - i \sum_{ij} M_{ij}^\gamma c_n c_i^\dagger c_j \quad (\text{A27})$$

We assume that the phonon cloud is at equilibrium at temperature T , so $\langle b_\beta b_\gamma \rangle = 0$. Now, simplifying by taking expectation values in place of product of multiplication of operator. This is similar to a mean field approximation,

$$\frac{d}{dt} C_{n\gamma}^{ph}(t) + i\omega_\gamma C_{n\gamma}^{ph}(t) + i \sum_j H_{nj} C_{j\gamma}^{ph}(t) = -i \sum_{ij\beta} M_{ij}^\beta \langle b_\beta^\dagger b_\gamma \rangle \delta_{ni} c_j - i \sum_{ij\beta} M_{ij}^\beta \langle c_n c_i^\dagger \rangle \delta_{\beta\gamma} c_j \quad (\text{A28})$$

Using the commutation and anitcommutation relation for Boson and Fermions respectively and substituting for the delta functions, we get,

$$\begin{aligned} \frac{d}{dt} C_{n\gamma}^{ph}(t) + i\omega_\gamma C_{n\gamma}^{ph}(t) + i \sum_j H_{nj} C_{j\gamma}^{ph}(t) &= -i \sum_{ij\beta} M_{ij}^\beta \left(\langle c_i^\dagger(t) c_n(t) \rangle \langle b_\beta^\dagger(t) b_\gamma(t) \rangle \right. \\ &\quad \left. + \langle c_n(t) c_i^\dagger(t) \rangle \langle b_\gamma(t) b_\beta^\dagger(t) \rangle \right) c_j(t). \end{aligned} \quad (\text{A29})$$

Using the retarded propagator for the composite operator,

$$g_{1,\gamma}^{ph}(t - t') \equiv -i \Theta(t - t') e^{-i(\omega_\gamma + H)(t - t')}. \quad (\text{A30})$$

The formal solution of the above equation reads,

$$\begin{aligned} C_{n\gamma}^{ph}(t) &= C_{n\gamma}^{0ph}(t) \\ &\quad - i \int_{t_0}^t dt' \sum_{ij\beta} M_{ij}^\beta g_{1,n\gamma}^{ph}(t - t') \left(\langle c_i^\dagger(t') c_n(t') \rangle \langle b_\beta^\dagger(t') b_\gamma(t') \rangle + \langle c_n(t') c_i^\dagger(t') \rangle \langle b_\gamma(t') b_\beta^\dagger(t') \rangle \right) c_j(t'). \end{aligned} \quad (\text{A31})$$

Taking the lowest order approximation in the electron phonon interaction matrix M^β , we can take, $g_{1,n\gamma}^{ph}(t - t') c_n(t') b_\gamma(t') \approx c_n(t) b_\gamma(t)$ inside the integral. So,

$$\begin{aligned} C_{n\gamma}^{ph}(t) &\approx C_{n\gamma}^{0ph}(t) \\ &\quad - i \int_{t_0}^t dt' \Theta(t - t') \sum_{ij\beta} M_{ij}^\beta \left(\langle c_i^\dagger(t') c_n(t) \rangle \langle b_\beta^\dagger(t') b_\gamma(t) \rangle + \langle c_n(t) c_i^\dagger(t') \rangle \langle b_\gamma(t) b_\beta^\dagger(t') \rangle \right) c_j(t') + \mathcal{O}[(M^\beta)^2] \end{aligned} \quad (\text{A32})$$

We now introduce the electronic correlation matrices,

$$G_{i,j}^N(t, t') \equiv \langle c_j^\dagger(t') c_i(t) \rangle, \quad G_{i,j}^P(t, t') \equiv \langle c_i(t) c_j^\dagger(t') \rangle, \quad (\text{A33})$$

$$B_{\gamma\beta}^{ab}(t, t') \equiv \langle b_\beta^\dagger(t') b_\gamma(t) \rangle, \quad (\text{A34})$$

$$B_{\gamma\beta}^{em}(t, t') \equiv \langle b_\gamma(t) b_\beta^\dagger(t') \rangle. \quad (\text{A35})$$

In thermal equilibrium at temperature T , these become (in the mode basis)

$$B_{\gamma\beta}^{ab}(t, t') = \delta_{\gamma\beta} e^{-i\omega_\gamma(t-t')} n_B(\omega_\gamma, T) \quad (\text{A36})$$

$$B_{\gamma\beta}^{em}(t, t') = \delta_{\gamma\beta} e^{-i\omega_\gamma(t-t')} (1 + n_B(\omega_\gamma, T)) \quad (\text{A37})$$

with the Bose function

$$n_B(\omega, T) = \frac{1}{e^{\omega/T} - 1}. \quad (\text{A38})$$

In the equilibrium phonon basis, the sum over β collapses due to $B_{\gamma\beta} \propto \delta_{\gamma\beta}$. Writing this explicitly we obtain,

$$\begin{aligned} |C_\gamma^{ph}(t)\rangle &= |C_\gamma^{0ph}(t)\rangle \\ &\quad - i \int_{t_0}^t dt' \Theta(t - t') e^{-i\omega_\gamma(t-t')} \left(n_B(\omega_\gamma, T) G^N(t, t') + (1 + n_B(\omega_\gamma, T)) G^P(t, t') \right) M^\gamma |c(t')\rangle. \end{aligned} \quad (\text{A39})$$

A completely analogous derivation for the operator $K_{n\gamma}^{ph}(t) \equiv c_n(t) b_\gamma^\dagger(t)$ gives

$$\begin{aligned} |K_\gamma^{ph}(t)\rangle &= |K_\gamma^{0ph}(t)\rangle \\ &\quad - i \int_{t_0}^t dt' \Theta(t - t') e^{i\omega_\gamma(t-t')} \left(n_B(\omega_\gamma, T) G^P(t, t') + (1 + n_B(\omega_\gamma, T)) G^N(t, t') \right) M^\gamma |c(t')\rangle. \end{aligned} \quad (\text{A40})$$

Together, Eqs. (A39) and (A40) encode the influence of the phonon bath on the electronic system in terms of equilibrium Bose factors, electronic correlation functions, and the composite propagator $g_{1,\gamma}^{ph}$.

Now we define the noise and damping term due to the electron phonon coupling. First the noise terms,

$$|\eta_{\gamma}^{ph}(t, t_0)\rangle = M^{\gamma} \left(g_{1,\gamma}^{ph}(t - t') |C_{\gamma}^{ph}(t_0)\rangle + g_{2,\gamma}^{ph}(t - t_0) |K_{\gamma}^{ph}(t_0)\rangle \right) \quad (\text{A41})$$

where ' $g_{2,\gamma}^{ph}(t - t_0)$ ' is the retarded propagator for $|K_{\gamma}^{ph}(t_0)\rangle$. The damping term is given as,

$$\begin{aligned} \Sigma_{\gamma}^{r,ph}(t - t') &= \Theta(t - t') \left[e^{-i\omega_{\gamma}(t - t')} M^{\gamma} \left(n_B(\omega_{\gamma}, T) G^N(t, t') + (1 + n_B(\omega_{\gamma}, T)) G^P(t, t') \right) M^{\gamma} \right. \\ &\quad \left. + e^{i\omega_{\gamma}(t - t')} M^{\gamma} \left(n_B(\omega_{\gamma}, T) G^P(t, t') + (1 + n_B(\omega_{\gamma}, T)) G^N(t, t') \right) M^{\gamma} \right] \end{aligned} \quad (\text{A42})$$

Now putting this in the equation of motion of the fermion operator of system of interest in (A21),

$$\begin{aligned} |\dot{c}\rangle &= -iH|c\rangle - i \sum_{\beta} |\eta_{\beta}^{ph}\rangle - i \sum_{\beta} \int_{t_0}^t dt' \Sigma_{\beta}^{r,ph}(t - t') |c(t')\rangle \\ &\quad - i|\eta_L\rangle - i \int_{t_0}^t dt' \Sigma_L^r(t - t') |c(t')\rangle - i|\eta_R\rangle - i \int_{t_0}^t dt' \Sigma_R^r(t - t') |c(t')\rangle \end{aligned} \quad (\text{A43})$$

We know from the standard Langevin equation analysis that once we have all the noise and damping terms we can find the time dependent inscattering matrices³⁴.

$$\begin{aligned} \Gamma^{ph}(t, t') &= \sum_{\gamma} M^{\gamma} \left(e^{-i\omega_{\gamma}(t - t')} n_B(\omega_{\gamma}, T) G^N(t, t') + e^{-i\omega_{\gamma}(t - t')} (1 + n_B(\omega_{\gamma}, T)) G^P(t, t') \right. \\ &\quad \left. + e^{i\omega_{\gamma}(t - t')} n_B(\omega_{\gamma}, T) G^P(t, t') + e^{i\omega_{\gamma}(t - t')} (1 + n_B(\omega_{\gamma}, T)) G^N(t, t') \right) M^{\gamma}. \end{aligned} \quad (\text{A44})$$

The in-scattering (lesser) self-energy due to phonons is defined from the noise correlator as,

$$\Sigma_{ij}^{<,ph}(t, t') = i \sum_{\gamma} \langle \eta_{\gamma,j}^{\dagger,ph}(t') \eta_{\gamma,i}^{ph}(t) \rangle \quad (\text{A45})$$

Substituting (A41) and expanding, we obtain

$$\begin{aligned} \Sigma_{ij}^{<,ph}(t, t') &\approx i \sum_{\gamma} \sum_{mn} M_{im}^{\gamma} M_{nj}^{\gamma} \left[\langle C_{n\gamma}^{ph\dagger}(t') C_{m\gamma}^{ph}(t) \rangle + \langle K_{n\gamma}^{ph\dagger}(t') C_{m\gamma}^{ph}(t) \rangle \right. \\ &\quad \left. + \langle C_{n\gamma}^{ph\dagger}(t') K_{m\gamma}^{ph}(t) \rangle + \langle K_{n\gamma}^{ph\dagger}(t') K_{m\gamma}^{ph}(t) \rangle \right]. \end{aligned} \quad (\text{A46})$$

Each average factorizes into an electronic and a phononic part. For example,

$$\langle C_{n\gamma}^{ph\dagger}(t') C_{m\gamma}^{ph}(t) \rangle = \langle c_n^{\dagger}(t') b_{\gamma}^{\dagger}(t') b_{\gamma}(t) c_m(t) \rangle \simeq \langle c_n^{\dagger}(t') c_m(t) \rangle \langle b_{\gamma}^{\dagger}(t') b_{\gamma}(t) \rangle, \quad (\text{A47})$$

and similarly for the other three terms. Using the definitions,

$$G_{m,n}^N(t, t') = \langle c_n^{\dagger}(t') c_m(t) \rangle, \quad G_{m,n}^P(t, t') = \langle c_m(t) c_n^{\dagger}(t') \rangle, \quad (\text{A48})$$

$$B_{\gamma\gamma}^{ab}(t, t') = \langle b_{\gamma}^{\dagger}(t') b_{\gamma}(t) \rangle, \quad B_{\gamma\gamma}^{em}(t, t') = \langle b_{\gamma}(t) b_{\gamma}^{\dagger}(t') \rangle, \quad (\text{A49})$$

one finds that the noise correlator can be written compactly as

$$\Sigma_{ph}^{<}(t, t') = i \sum_{\gamma} M^{\gamma} \left[G^N(t, t') B_{\gamma\gamma}^{em}(t, t') + G^N(t, t') B_{\gamma\gamma}^{ab}(t', t) \right] M^{\gamma}. \quad (\text{A50})$$

Taking the equilibrium form for the Boson operators like earlier, the explicit form of the e-ph in-scattering self-energy,

$$\Sigma_{ph}^{<}(t, t') = i \sum_{\gamma} M^{\gamma} \left[(1 + n_B(\omega_{\gamma}, T)) G^N(t, t') e^{-i\omega_{\gamma}(t - t')} + n_B(\omega_{\gamma}, T) G^N(t, t') e^{+i\omega_{\gamma}(t - t')} \right] M^{\gamma}. \quad (\text{A51})$$

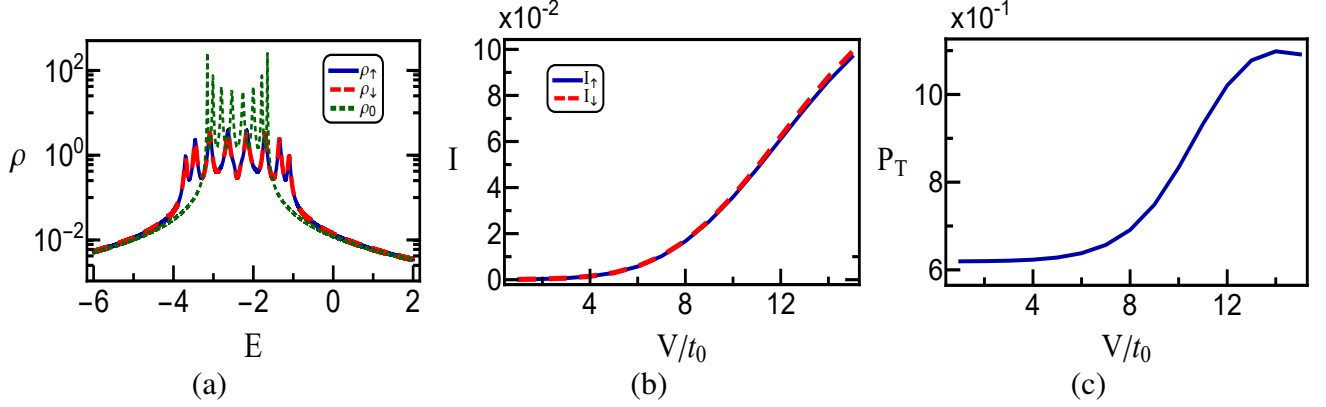


FIG. 5: (a) Energy-dependent density of states obtained using the approximations introduced in Appendix B, (b) Current-voltage characteristics for opposite left-lead magnetizations. (c) Spin polarization as a function of bias voltage.

Finally to obtain the steady state results we use the Fourier transform similar to the study³⁴ and use the standard lesser/greater Green's functions $G^{</>}$, $G^<(t, t') = iG^N(t, t')$ and $G^>(t, t') = -iG^P(t, t')$, the same expression can be cast in the more familiar form given in the section III.

$$\begin{aligned} \Gamma_{\text{ph}}(E) &= i \sum_{\gamma} M^{\gamma} \left(-n_B(\omega_{\gamma}, T) G^<(E - \omega_{\gamma}) + (1 + n_B(\omega_{\gamma}, T)) G^>(E - \omega_{\gamma}) \right. \\ &\quad \left. + n_B(\omega_{\gamma}, T) G^>(E + \omega_{\gamma}) - (1 + n_B(\omega_{\gamma}, T)) G^<(E + \omega_{\gamma}) \right) M^{\gamma} \end{aligned} \quad (\text{A52})$$

$$\Sigma_{\text{ph}}^<(E) = \sum_{\gamma} M^{\gamma} \left(n_B(\omega_{\gamma}, T) G^<(E - \omega_{\gamma}) + (1 + n_B(\omega_{\gamma}, T)) G^<(E + \omega_{\gamma}) \right) M^{\gamma} \quad (\text{A53})$$

Appendix B: Fransson's approximation of equilibrium e-ph bath²⁸

This involves simplifying the broadening matrix. To do this it is assumed that the Green's Functions at energies $E \pm \omega$ can be approximated by their equilibrium values. Further these equilibrium values are just taken by considering the on site energy ϵ_0 . This means that the energy shifted Green's Functions are just considered as, $G^<(E) = 2i\pi\delta(E - \epsilon_0)f_0(\epsilon_0)$, $G^>(E) = -2i\pi\delta(E - \epsilon_0)(1 - f_0(\epsilon_0))$. Using this in the expression for broadening matrix, and then doing the appropriate Hilbert transform of the delta function to get the lesser self energy, we get the following expression for the retarded Green's Function at energy E ,^{28,35},

$$G^R(E) = \left(E - H - \Sigma(E)H_1^2 + \frac{i}{2}(\Gamma^L + \Gamma^R) \right)^{-1}, \quad (\text{B1})$$

The self-energy due to first order e-ph interactions is,

$$\Sigma(E) = \frac{n_B(\omega_0) + 1 - f(\epsilon)}{E - \omega_0 - \epsilon + i\eta} + \frac{n_B(\omega_0) + f(\epsilon)}{E + \omega_0 - \epsilon + i\eta}. \quad (\text{B2})$$

where η is a parameter used for denoting internal broadening due to electron phonon interaction, $\eta = \frac{t_0}{4}$. This is the simplification assumed in the analysis by Fransson in various studies^{16,28}. Additionally, the contribution of electron phonon coupling to the density of occupied electronic states is neglected and it is simply given as,

$$G^<(E) = i \left(f_L G^R \Gamma_L G^A + f_R G^R \Gamma_R G^A \right) \quad (\text{B3})$$

1. Current and density in Fransson's analysis

We next present the results obtained by analysing the model using Fransson's approximations, shown in Fig. 5. In Fig. 5(a), we observe that, similar to the fully self-consistent analysis, the density of states spreads out in the presence of electron-phonon

interactions. The inclusion of interactions leads to a redistribution of spectral weight over a wider energy range, indicating that inelastic processes again play an important role in shaping the electronic structure. However, there is a significant qualitative difference compared to the self-consistent case. In particular, the individual resonant peaks in the DOS remain clearly visible when Fransson's approximations are employed, in contrast to the strongly smeared spectrum obtained in the self-consistent treatment. This difference highlights the sensitivity of the spectral properties to the level of approximation used in treating electron-phonon interactions.

The corresponding particle current is shown in Fig. 5(b). As compared to the self-consistent case, the overall magnitude of the current remains small. However, for larger voltages we can see a visible distinction between the two currents at opposite lead magnetization. Finally, we plot the spin polarization as a function of bias voltage in Fig. 5(c). Unlike the self-consistent analysis, a finite polarization is observed within this approximation scheme. This indicates that the use of Fransson's approximations leads to qualitatively different conclusions regarding the emergence of spin-selective transport, despite the overall current remaining small.

¹K. Ray, S. P. Ananthavel, D. H. Waldeck, and R. Naaman, "Asymmetric scattering of polarized electrons by organized organic films of chiral molecules," *Science* **283**, 814–816 (1999).

²B. Göhler, V. Hamelbeck, T. Z. Markus, M. Kettner, G. F. Hanne, Z. Vager, R. Naaman, and H. Zacharias, "Spin selectivity in electron transmission through self-assembled monolayers of double-stranded dna," *Science* **331**, 894–897 (2011).

³Z. Xie, T. Z. Markus, S. R. Cohen, Z. Vager, R. Gutierrez, and R. Naaman, "Spin specific electron conduction through dna oligomers," *Nano Letters* **11**, 4652–4655 (2011).

⁴P. C. Mondal, C. Fontanesi, D. H. Waldeck, and R. Naaman, "Spin-dependent transport through chiral molecules studied by spin-dependent electrochemistry," *Accounts of Chemical Research* **49**, 2560–2568 (2016).

⁵D. Mishra, T. Z. Markus, R. Naaman, M. Kettner, B. Göhler, H. Zacharias, N. Friedman, M. Sheves, and C. Fontanesi, "Spin-dependent electron transmission through bacteriorhodopsin embedded in purple membrane," *Proceedings of the National Academy of Sciences of the United States of America* **110**, 14872–6 (2013).

⁶B. P. Bloom, Y. Paltiel, R. Naaman, and D. H. Waldeck, "Chiral induced spin selectivity," *Chemical Reviews* **124**, 1950–1991 (2024), pMID: 38364021.

⁷R. Naaman, Y. Paltiel, and D. H. Waldeck, "Chiral molecules and the spin selectivity effect," *The Journal of Physical Chemistry Letters* **11**, 3660–3666 (2020).

⁸R. Gutierrez, E. Díaz, R. Naaman, and G. Cuniberti, "Spin-selective transport through helical molecular systems," *Phys. Rev. B* **85**, 081404 (2012).

⁹A.-M. Guo and Q.-f. Sun, "Spin-selective transport of electrons in dna double helix," *Phys. Rev. Lett.* **108**, 218102 (2012).

¹⁰F. Evers, A. Aharony, N. Bar-Gill, O. Entin-Wohlman, P. Hedegård, O. Hod, P. Jelinek, G. Kamienski, M. Lemeshko, K. Michaeli, V. Mujica, R. Naaman, Y. Paltiel, S. Refaeli-Abramson, O. Tal, J. Thijssen, M. Thoss, J. M. van Ruitenbeek, L. Venkataraman, D. H. Waldeck, B. Yan, and L. Kronik, "Theory of chirality induced spin selectivity: Progress and challenges," *Advanced Materials* **34**, 2106629 (2022).

¹¹S. Yeganeh, M. A. Ratner, E. Medina, and V. Mujica, "Chiral electron transport: Scattering through helical potentials," *The Journal of Chemical Physics* **131**, 014707 (2009).

¹²L. Barron, "True and false chirality and parity violation," *Chemical Physics Letters* **123**, 423–427 (1986).

¹³L. Onsager, "Reciprocal relations in irreversible processes. i," *Physical review* **37**, 405 (1931).

¹⁴J. H. Bardarson, "A proof of the kramers degeneracy of transmission eigenvalues from antisymmetry of the scattering matrix," *Journal of Physics A: Mathematical and Theoretical* **41**, 405203 (2008).

¹⁵H. B. G. Casimir, "On onsager's principle of microscopic reversibility," *Reviews of Modern Physics* **17**, 343 (1945).

¹⁶J. Fransson, "The chiral induced spin selectivity effect what it is, what it is not, and why it matters," *Israel Journal of Chemistry* **62**, e202200046 (2022).

¹⁷S. Varela, M. Peralta, V. Mujica, B. Berche, and E. Medina, "Spin polarization induced by decoherence in a tunneling one-dimensional Rashba model," *SciPost Phys. Core* **6**, 044 (2023).

¹⁸A. Aharony and O. Entin-Wohlman, "Spin–orbit interactions, time-reversal symmetry, and spin selection," *The Journal of Chemical Physics* **162**, 154103 (2025).

¹⁹Y. Utsumi, O. Entin-Wohlman, and A. Aharony, "Spin selectivity through time-reversal symmetric helical junctions," *Phys. Rev. B* **102**, 035445 (2020).

²⁰M. Kilgour and D. Segal, "Charge transport in molecular junctions: From tunneling to hopping with the probe technique," *The Journal of Chemical Physics* **143**, 024111 (2015).

²¹A. G. Volosniev, H. Alpern, Y. Paltiel, O. Millo, M. Lemeshko, and A. Ghazaryan, "Interplay between friction and spin-orbit coupling as a source of spin polarization," *Phys. Rev. B* **104**, 024430 (2021).

²²S. Alwan and Y. Dubi, "Spinterface origin for the chirality-induced spin-selectivity effect," *Journal of the American Chemical Society* **143**, 14235–14241 (2021).

²³S. Sarkar, A. Sharoni, O. L. Monti, and Y. Dubi, "The spinterface mechanism for the chiral-induced spin selectivity effect: A critical perspective," *ACS nano* **19**, 37484–37503 (2025).

²⁴H.-H. Teh, W. Dou, and J. E. Subotnik, "Spin polarization through a molecular junction based on nuclear berry curvature effects," *Phys. Rev. B* **106**, 184302 (2022).

²⁵J. Fransson, "Chirality-induced spin selectivity: The role of electron correlations," *The Journal of Physical Chemistry Letters* **10**, 7126–7132 (2019), pMID: 31657931.

²⁶A. Chiesa, E. Garlatti, M. Mezzadri, L. Celada, R. Sessoli, M. R. Wasielewski, R. Bittl, P. Santini, and S. Carretta, "Many-body models for chirality-induced spin selectivity in electron transfer," *Nano Letters* **24**, 12133–12139 (2024).

²⁷J. Fransson, "Should it really be that hard to model the chirality induced spin selectivity effect?" *APL Computational Physics* **1**, 020903 (2025).

²⁸J. Fransson, "Vibrational origin of exchange splitting and "chiral-induced spin selectivity," *Phys. Rev. B* **102**, 235416 (2020).

²⁹J. Han, Y. Wang, and W. Dou, "Mixed quantum–classical approaches to electron transmission through chiral molecules," *Chinese Journal of Chemical Physics* (2025).

³⁰R. Smorka, S. L. Rudge, and M. Thoss, "Influence of nonequilibrium vibrational dynamics on spin selectivity in chiral molecular junctions," *The Journal of Chemical Physics* **162**, 014304 (2025).

³¹M. Paulsson, T. Frederiksen, and M. Brandbyge, "Modeling inelastic phonon scattering in atomic- and molecular-wire junctions," *Phys. Rev. B* **72**, 201101 (2005).

³²M. Galperin, M. A. Ratner, and A. Nitzan, "Molecular transport junctions: vibrational effects," *Journal of Physics: Condensed Matter* **19**, 103201 (2007).

³³T. Holstein, "Studies of polaron motion: Part i. the molecular-crystal model," *Annals of Physics* **8**, 325–342 (1959).

³⁴A. Dhar and D. Sen, "Nonequilibrium green's function formalism and the problem of bound states," *Phys. Rev. B* **73**, 085119 (2006).

³⁵S. Datta, *Quantum Transport: Atom to Transistor* (Cambridge University Press, 2005).

³⁶R. Landauer, "Spatial variation of currents and fields due to localized scatterers in metallic conduction," *IBM Journal of research and development* **1**, 223–231 (1957).

³⁷M. Büttiker, "Four-terminal phase-coherent conductance," *Physical review letters* **57**, 1761 (1986).

³⁸M. Saha, B. K. Agarwalla, M. Kulkarni, and A. Purkayastha, "Univer-

sal subdiffusive behavior at band edges from transfer matrix exceptional points,” *Phys. Rev. Lett.* **130**, 187101 (2023).

³⁹Y. Meir and N. S. Wingreen, “Landauer formula for the current through an interacting electron region,” *Physical review letters* **68**, 2512 (1992).

⁴⁰A.-P. Jauho, N. S. Wingreen, and Y. Meir, “Time-dependent transport in interacting and noninteracting resonant-tunneling systems,” *Physical Review B* **50**, 5528 (1994).

⁴¹T. Frederiksen, M. Paulsson, M. Brandbyge, and A.-P. Jauho, “Inelastic transport theory from first principles: Methodology and application to nanoscale devices,” *Phys. Rev. B* **75**, 205413 (2007).

⁴²P. Pulay, “Convergence acceleration of iterative sequences. the case of scf iteration,” *Chemical Physics Letters* **73**, 393–398 (1980).

⁴³J. Fransson, “Chiral induced spin polarized electron current: Origin of the chiral induced spin selectivity effect,” *The Journal of Physical Chemistry Letters* **16**, 4346–4353 (2025), pMID: 40270227.

⁴⁴R. Golizadeh-Mojarad and S. Datta, “Nonequilibrium green’s function based models for dephasing in quantum transport,” *Phys. Rev. B* **75**, 081301 (2007).

⁴⁵M. Büttiker, “Role of quantum coherence in series resistors,” *Physical Review B* **33**, 3020 (1986).

⁴⁶S. Alwan, S. Sarkar, A. Sharoni, and Y. Dubi, “Temperature-dependence of the chirality-induced spin selectivity effect—experiments and theory,” *The Journal of Chemical Physics* **159**, 014106 (2023).